Temporal coherence of the Ni-like palladium x-ray laser in the transient pumping scheme

D. Benredjem, C. Möller, and J. Dubau
LIXAM, Faculté des Sciences d'Orsay, Bâtiment 350, Université de Paris-Sud, 91405 Orsay, France

T. Ball
Department of Physics, University of York, York, YO10 5DD, United Kingdom

(Received 16 November 2005; revised manuscript received 30 January 2006; published 20 June 2006)

In this paper, we present results on the temporal coherence of the Ni-like palladium x-ray laser. We have modeled an experiment performed at the COMET laser facility (Lawrence Livermore National Laboratory), in order to investigate the coherence properties of the line at wavelength 14.68 nm ($4d\ ^1S_0 \rightarrow 4p\ ^1P_1$ transition). To this end, a ray-tracing postprocessor is coupled to a collisional-radiative code. The effect of saturation on gain coefficient values is taken into account by developing a rigorous approach based on the Maxwell-Bloch formalism. The temporal coherence depends strongly on the shape and width of the amplified line. Our calculations give a coherence length of 290 μm. While the full width at half maximum of the optically thin line is 28 mÅ, the amplified x-ray line exhibits a Gaussian profile and a width of 4 mÅ. Calculated coherence lengths and gains agree with measurements. Comparison with experiment is discussed.

DOI: 10.1103/PhysRevA.73.063820 PACS number(s): 42.55.Vc, 42.15.Dp, 42.50.Ar

I. INTRODUCTION

In the standard quasi-steady-state (QSS) scheme, a solid target is irradiated by a relatively long pulse (100–600 ps) preceded by one or several low-energy pulses (prepulses). The pulse—focused onto a line—produces a near-cylindrical plasma column and creates population inversion. Saturated gain-length products greater than 20 are routinely reached with net pump energies below 500 J (see, e.g., Ref. [1]).

During the last decade considerable progress has been made in the reduction of the necessary pump energy, in order to produce small-size driving lasers. The energy requirements were dramatically reduced to a few joules after the development of a promising new scheme [2]. This so-called transient scheme consists in a two-stage target irradiation. First, a low-intensity pulse of 300–600 ps duration creates a plasma with a large proportion of the desired ion species, i.e., Ne-like or Ni-like. Then, a high-intensity, picosecond pulse heats the preformed plasma. As a result, transient population inversions are obtained, due to collisions between free electrons and ions. Since the high-intensity plasma is short lived ($\sim$10 ps) compared to the photon propagation time in the amplifying medium ($\sim$33 ps for a 1-cm-long target), the short pulse must heat the plasma only locally and make the gain region travel at the velocity of x-ray-laser (XRL) photons. This is known as the traveling-wave (TW) irradiation geometry. This irradiation type, whose beneficial effect was demonstrated by Tallents *et al.* [3], produces strong amplification. For a 400 fs heating pulse, the XRL output intensity was enhanced by a factor of 300–400 compared to the non-TW irradiation.

Transient XRL experiments, including those on Ni-like Ag, were simulated numerically by several authors [4–6]. Results are in qualitatively good agreement with experiments. However, calculated gains are one order of magnitude higher than measured gains. In a recent work on silver [7], we used an approach based on the Maxwell-Bloch (MB) formalism (see, for example, [8,9]), in which the saturation effect is treated rigorously. Refraction of the XRL beam in large electron-density gradients is also taken into account. This approach yields more reasonable gain coefficients: $\sim$140 cm^{-1} instead of $\sim$800 cm^{-1} with collisional-radiative codes neglecting saturation.

The rapid development of XRLs combined with the availability of optics in the extreme uv range induced many applications, such as in interferometry [10–12], holography [13], and interferometric microscopy [14]. These applications were made possible due to the coherence properties of x-ray pulses.

The temporal coherence of the Ni-like silver laser at wavelength 13.9 nm was recently investigated by using a new Fresnel interferometer [15]. A coherence time of $\approx$2.8 ps (coherence length $\approx$840 μm), corresponding to a full width at half maximum (FWHM) of 0.7 mÅ, was measured. Previous experiments had been performed at the Lawrence Livermore National Laboratory, on the NOVA Ne-like Y XRL at wavelength 15.5 nm [16], and on the COMET Ni-like Pd XRL at wavelength 14.68 nm [17]. In the first experiment, a QSS plasma was obtained with a single 500 ps pulse with multikilojoule energy. A coherence length of 100 μm (coherence time $\approx$0.33 ps), corresponding to a FWHM of 13 mÅ for the amplified line, was obtained with a Mach-Zender interferometer. In the second experiment, a 1.25-cm-long polished Pd slab target was irradiated in the TW geometry along a 1.6-cm-long line focus. An optical pumping combination of a 600- (2 J, 2×10^{11} W/cm^2) and a 13-ps-long-pulse (5 J, 3×10^{13} W/cm^2) yielded a saturated XRL output of 10 μJ. A longitudinal coherence length of $\sim$400 μm was measured by using amplitude division geometry. The coherence time is thus 1.3 ps. The amplified line exhibits a Gaussian shape with a FWHM $\sim$2.9 mÅ (a factor 4 less than in the QSS scheme, mainly due to lower ion temperature).

In Sec. II, we use the collisional-radiative code EHYBRID [18] to calculate the gain coefficient, electron density, and electron and ion temperatures as functions of time and distance from the target surface. To account for refraction, a

 ©2006 The American Physical Society

ray-trace postprocessor is coupled to EHYBRID. The saturation effect is taken into account by a simple method, and the intensity spectrum is calculated for various plasma lengths. Knowing the intensity profile, it is not difficult to obtain the coherence length. In Sec. III, an alternative approach describing more rigorously the saturation effect on level populations is used. It involves the Maxwell-Bloch formalism. Refraction is taken into account. This approach gives the same coherence length as the first one but has the advantage of providing a gain value in satisfactory agreement with experiment.

II. RAY-TRACE CALCULATIONS

A. Gain calculated with EHYBRID

The first step of our modeling of the experiment described in Ref. [17] concerns gain variation with time and distance from target surface. We use the hydrodynamic-atomic package EHYBRID developed by Pert [18] to understand the amplifying medium evolution. EHYBRID accounts for physical processes such as pump-laser energy deposition, hydrodynamic motion, electronic thermal conduction, and ion-electron thermalization, which are coupled with the atomic physics of the lasing ion. The atomic database involves a set of 382 levels including all levels of the $n=4-5$ manifolds, and averaged contributions from the $n=6-7$ levels. Oscillator strengths for all transitions in the $n=4-7$ manifolds were calculated with a multiconfigurational Dirac-Fock code [19]. Electron-ion collision rates are obtained by the standard fitting procedure involving d coefficients [20]. The model is 1.5D and the plasma expansion occurs in the direction of the pump laser with cells (294 Lagrangian cells) that are assumed to be laterally isothermal: the transverse expansion is assumed to be self-similar. The calculation of the ionization balance, and in particular the abundance of nickellike ions, is very important in these calculations. In each cell, the ionization kinetics is calculated using a collisional-radiative model which represents the most sophisticated treatment available of time-dependent atomic physics in plasmas. Electron-ion collision (excitation, deexcitation, and ionization) and recombination (three-body, radiative, and dielectronic) processes are included in the coupled rate equations for each ionic level. Radiative losses are taken into account. Radiation trapping is taken into account through escape factors that can be controlled in the input file. A great challenge in EHYBRID is the absence of radiative processes involving the x-ray line, such as absorption and induced emission.

Figure 1 shows the gain coefficient of the $4d\ ^1S_0-4p\ ^1P_1$ line at wavelength 14.7 nm, as a function of time and distance from the target surface. The long pulse (FWHM 600 ps) is followed by the short pulse (FWHM 13 ps) with a 700 ps peak-to-peak delay. Two distinct regions are predicted. After the short pulse is turned on, a high-gain region ($>200\ \mathrm{cm}^{-1}$) emerges with small dimensions in both space (within $5-10\ \mu$m from the target surface) and time (~ 10 ps). Later, after the laser is turned off, a large plateau with gains in the range $50-150\ \mathrm{cm}^{-1}$ extending out to $\sim 20\ \mu$m is observed.

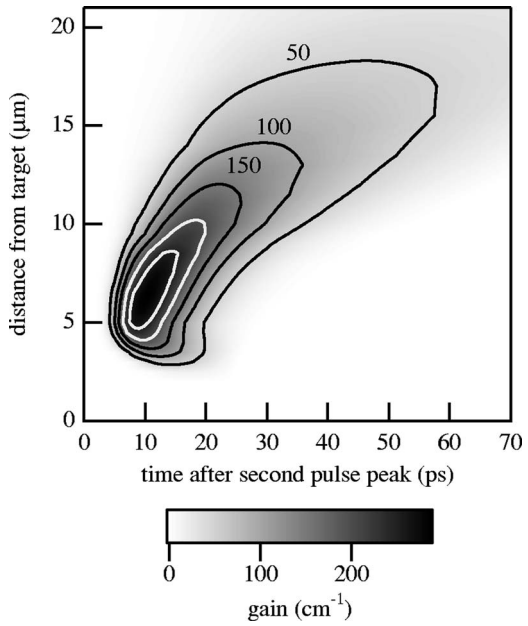

FIG. 1. Gain coefficient of the 0-1 line in Ni-like Pd, as a function of time and distance from the target surface. Only positive gains are represented. Contour lines are drawn for gain coefficients of 50 cm^{-1}, and further consecutive steps of 50 cm^{-1}. Results are obtained by modeling the experiment performed at LLNL [17] with the EHYBRID code. The origin of time is taken to be the peak of the short pulse whose duration (FWHM) is 13 ps. The peak-to-peak delay is equal to 700 ps.

By comparing the gain plot with the electron density plot (Fig. 2), we can see that the gain peaks at electron densities close to $10^{21}\ \mathrm{cm}^{-3}$. This is the critical density of the 1.06 μm laser driver and coincides spatially with a region of steep density gradients. Therefore, it would be expected that spatial sampling of this region would be limited by refraction. However, it is observed that the density gradients become more relaxed at distances farther away from the critical density surface and so, because of reduced refraction effects, a larger region of lower gain is expected to contribute to the XRL output.

Figure 3 shows the variation of electron and ion temperatures with time and distance from target surface. In the region of peak gain, the ion temperature [Fig. 3(a)] falls within the 40–50 eV range. Doppler broadening is then expected to be small. After the main pulse is turned off, the bulk of the plasma stays hot (electron temperatures above 200 eV) for approximately 10 ps. This prolonged heating causes the average ionization of the plasma to increase rapidly. Electron temperatures greater than 250 eV coexist spatially and temporally with high gains. The temperature gradients are similar to those observed on Ni-like Ag [5] with quick dissipation from a small intense region into a larger more uniform plateau with temperatures below 150 eV.

In the following sections, we describe two approaches aimed at giving the intensity spectrum of the x-ray beam and the coherence length. In the first one, we use the geometric approximation, and a ray-trace code is constructed as a postprocessor of EHYBRID. The knowledge of the gain coefficient, emissivity, and saturation intensity from EHYBRID al-

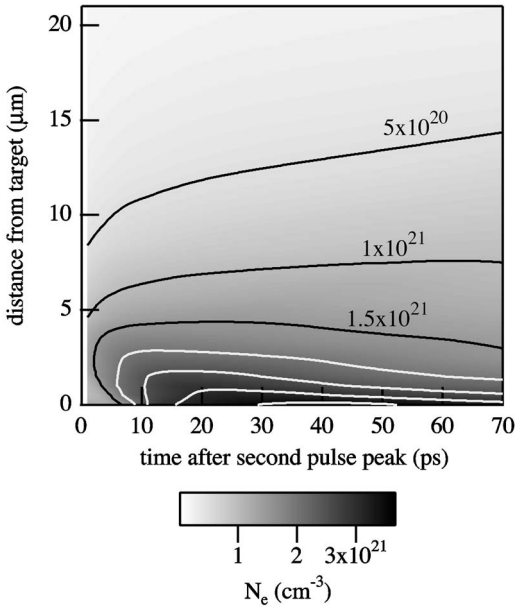

FIG. 2. Evolution of free-electron density with time and distance from the target surface. Contour lines are drawn for 5×10^{20}, 10^{21}, 1.5×10^{21} cm^{-3}, and further consecutive steps of 5×10^{20} cm^{-3}. Results are obtained by modeling the experiment performed at LLNL [17] with the EHYBRID code. Origin of time and peak-to-peak delay as in Fig. 1.

lows us to account for saturation effects. The second approach, based on the paraxial MB formalism, treats the saturation effect on Ni-like level populations more rigorously.

B. First approach: Ray-tracing and saturation effect

Since electron density gradients are steeper in transient XRLs [4,5] than in the QSS scheme using the multipulse technique with ~100 ps duration for the main pulse, refraction becomes a substantial issue, dramatically limiting amplification. In fact, Figs. 1 and 2 show that the substantial gain values are confined in a region of small extension ~10 μm, very close to the target surface, where the electron density is near 10^{21} cm^{-3}. This is the critical density surface of the 1.06 μm driving laser and coincides spatially with a region of steep density gradients. As a result, the beam is expected to leave the zone of maximum amplification before reaching the end of the target. On the other hand, given the large gain, XRLs operating in the transient scheme often saturate for plasma lengths $L\sim3-4$ mm. To address these two issues, we use a ray-trace code which accounts for saturation.

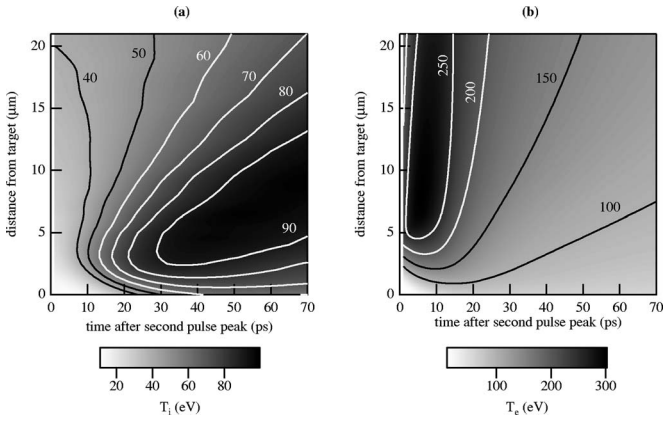

FIG. 3. Evolution of temperature with time and distance from the target surface. (a) Ion temperature with contour lines drawn for 40 eV and further consecutive steps of 10 eV; (b) electron temperature with contour lines drawn for 100 eV and further consecutive steps of 50 eV. Results are obtained by modeling the experiment performed at LLNL [17] with the EHYBRID code. Origin of time and peak-to-peak delay, as in Fig. 1.

The spectral intensity is given by the following relation which is valid in the small-signal regime as well as in the saturation regime:

$$I(s,\nu)=\frac{\epsilon(\nu)}{G(s,\nu)}\{\exp[G(s,\nu)\Delta s]-1\}+I(s-\Delta s,\nu)\exp[G(s,\nu)\Delta s], \quad (1)$$

where ν is the frequency, s the current ray path length, and Δs a small interval of the path. The emissivity ϵ and gain coefficient G are given by

$$\epsilon(\nu)=N_u h\nu_0\frac{\Omega}{4\pi}A_{ul}\Phi_{ul}(\nu), \quad G(s,\nu)=\frac{G_{ss}(\nu)}{1+I(s)/I_{\rm sat}}, \quad (2)$$

where $I(s)$ is the integrated intensity, Ω the solid angle of emission, A_{ul} the Einstein coefficient for spontaneous emission between the two lasing levels u and l, and $\Phi_{ul}(\nu)$ the spontaneous emission (optically thin) profile. N_u is the population density of u. The gain coefficient depends on the small-signal gain G_{ss} and on the intensity of saturation I_{sat} (both quantities are given by EHYBRID). The small-signal gain is given by $G_{ss}(\nu)=h\nu(B_{ul}/c)[N_u-(g_u/g_l)N_l]\Phi_{ul}(\nu)$, where B_{ul} is the Einstein coefficient for stimulated emission, and the g's are statistical weights.

Due to the irradiation geometry, the amplifying medium is nearly cylindrical, with the amplification of the x-ray beam roughly parallel to the cylinder axis. In a Cartesian coordinates system, the z axis is taken to be the cylinder axis, while the axes x and y are respectively perpendicular and parallel to the target surface. Plasma expansion occurs mainly along the x axis.

The knowledge of Φ_{ul} is very important in temporal coherence studies because it determines the intensity spectrum. In a previous study [7], we have shown that the ion Stark broadening is negligible for Ni-like 0-1 lines. Natural broadening is also negligible (for the Ni-like Pd line at 14.7 nm, FWHM 0.15 mÅ). The dominant broadening mechanisms are electron impact (homogeneous) broadening and Doppler frequency detuning (inhomogeneous broadening). The Voigt function then gives a good representation of the optically thin line. Knowledge of the electron density (N_e) and electron and ion temperatures (T_e and T_i) is needed for the calculation of Φ_{ul}.

Let us define two dimensionless coefficients: $a=\sqrt{\ln 2}\Delta\nu_{\rm L}/\Delta\nu_{\rm D}$ and $b=2\sqrt{\ln 2}\nu/\Delta\nu_{\rm D}$, where $\Delta\nu_{\rm D}$ and $\Delta\nu_{\rm L}$

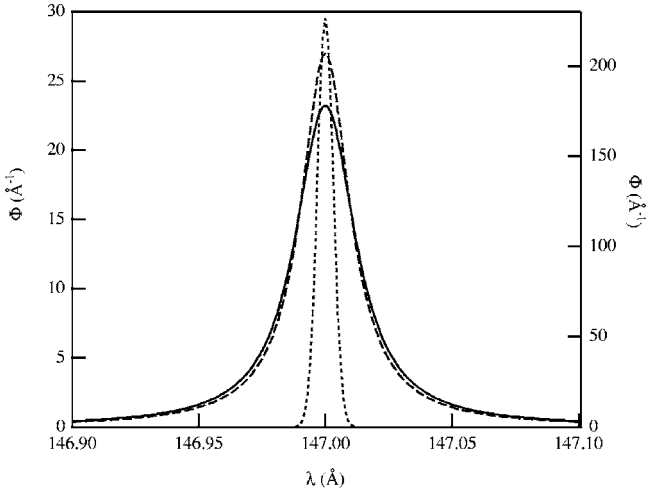

FIG. 4. Normalized profile of the optically thin line at 14.7 nm in Ni-like Pd. Full curve, Voigt profile (left scale); dashed curve, Lorentzian profile (left scale); dotted curve, Gaussian profile (right scale). The electron density and electron and ion temperature values used in the calculation correspond to the cell and time of peak gain. $G_{ss}(\nu_0)=287$ cm^{-1}, $N_e=1.1\times10^{21}$ cm^{-3}, $T_e=244$ eV, and $T_i=45$ eV, as given by EHYBRID.

are, respectively, the Doppler and Lorentz widths. a is the Voigt parameter. The normalized Voigt profile can be expressed in terms of the complementary error function of complex argument [21]. We have

$$\Phi_V(\nu)=\frac{1}{\sqrt{\pi}}\frac{2\sqrt{\ln 2}}{\Delta\nu_D}\,\mathrm{Re}[\exp(-z^2)\mathrm{erfc}(-iz)], \tag{3}$$

where $z=b+ia$. The calculation of Φ_V involves an expansion of the complex probability function, $\exp(-z^2)\mathrm{erfc}(-iz)$, due to Humlicek [22].

Figure 4 shows Φ_V as well as the Gaussian and Lorentzian profiles of the Ni-like Pd line at wavelength 14.7 nm. At the time and in the cell of peak gain, the EHYBRID code gives $G_{ss}(\nu_0)=287$ cm^{-1}, $N_e=1.1\times10^{21}$ cm^{-3}, $T_e=244$ eV, and $T_i=45$ eV, where ν_0 is the line peak frequency. Due to the high density values in the region of strong amplification, electron broadening overcomes Doppler broadening. The Voigt profile is thus very similar to the Lorentz profile. The FWHM associated with Doppler broadening is $\Delta\lambda_D=2\sqrt{2\ln 2}\lambda_{ul}\sqrt{kT_i/(Mc^2)}=7.35$ mÅ, where λ_{ul} is the wavelength of the lasing transition, M the ion mass, and c the velocity of light. Electron broadening yields a FWHM of 23.6 mÅ. The Voigt parameter is then equal to 2.67 and the Voigt profile FWHM to 28 mÅ.

Since Φ_{ul} is involved in emissivity and gain expressions, we have to update it during propagation. We have therefore implemented a subroutine giving the Voigt profile in our ray-trace code.

Figure 5 shows the intensity spectrum $I(\lambda)$ for two plasma lengths. For $L=0.1$ mm [Fig. 5(a)], the FWHM is 16 mÅ, a value to be compared to the 28 mÅ of the optically thin line. We have also fitted the intensity spectrum with Gaussian and Lorentzian functions. It is clear that the shape of $I(\lambda)$ is

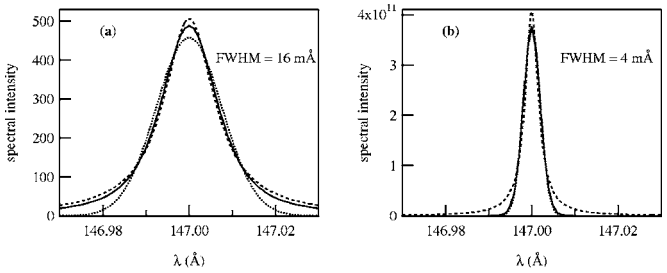

FIG. 5. Spectral intensity of the x-ray beam (full curve) and its Gaussian (dotted curve) and Lorentzian (dashed curve) fits. Plasma length $L=$(a) 0.1 and (b) 10 mm. Rays are launched at the time and from the cell of peak gain. Small-signal gain, electron density, and electron and ion temperature values at the onset of amplification as in Fig. 4.

practically Lorentzian. In fact, in the region of strong amplification, where the electron density reaches high values, homogeneous broadening overcomes ion thermal broadening. Figure 5(b) displays the intensity at the exit from the plasma, for $L=10$ mm. The intensity spectrum resulting from gain narrowing approaches a Gaussian shape, and its width is reduced to 4 mÅ. The profile determined from experiment is also Gaussian, its FWHM is above 2.9 mÅ, i.e., ~25% smaller than the calculated value.

The self-coherence at a point P is defined as the ensemble-averaged spatial correlation function [23]:

$$\Gamma(\tau)=\langle\mathbf{E}(P,t+\tau)\cdot\mathbf{E}^*(P,t)\rangle, \tag{4}$$

where $\mathbf{E}$ is the XRL electric field and τ a time delay between two perturbations—vibrations of the electric field—occurring in P. The angular brackets denote the time average. The Wiener-Khintchine theorem says that self-coherence and spectral density S form a Fourier transform pair. We then have

$$\Gamma(\tau)=4\int_0^\infty S(P,\nu)\exp(-2i\pi\nu\tau)d\nu. \tag{5}$$

In Appendix A, we show that if the shape of the spectral density (or the intensity) is Gaussian, then the shape of the self-coherence is also Gaussian. The $1/e$ half-width of Γ defines the coherence time, and the coherence length is given by $l_{coh}=c\tau_{coh}$. Our calculations give $l_{coh}=290$ μm, while measurements give ~400 μm.

This approach, where the saturation effect is treated by simple means provides (i) gains higher than 200 cm^{-1} (the measured gain is ~65 cm^{-1}), and (ii) too large integrated intensities. This shows that there is a need for an alternative approach in which the saturation effect is treated more rigorously.

III. SECOND APPROACH

A. Paraxial Maxwell-Bloch formalism

The Maxwell wave equation governing the evolution of the XRL electric field $\mathbf{E}$, in a globally neutral plasma, characterized by $\nabla\cdot\mathbf{E}=0$, is [9]

$$\left(\Delta - \frac{1}{c^2}\frac{\partial^2}{\partial t^2} - \frac{\omega_p^2}{c^2}\right)\mathbf{E} - \frac{1}{\epsilon_0 c^2}\frac{\partial^2}{\partial t^2}\mathbf{P} = 0, \tag{6}$$

where $\mathbf{P}$ is the atomic polarization and ω_p the electron plasma frequency. The term $(\omega_p^2/c^2)\mathbf{E}$ is obtained in the linear limit and if the bulk motion of the plasma can be neglected. It explains refraction and diffraction (see, e.g., Ref. [24]). The last contribution is due to the current density term $\partial\mathbf{P}/\partial t$ involving bound electrons. This contribution is responsible for spontaneous and induced emissions, and absorption. Basically, the difference between this approach and the first one resides in the fact that in the first approach the ray equation is obtained from the Maxwell wave equation where the bound electrons contribution is neglected. The polarization vector is given by $\mathbf{P}=\mathrm{Tr}(\rho\mathbf{d})$, where ρ is the density matrix and $\mathbf{d}$ the atomic electric dipole. These two quantities are related by the Bloch equation

$$i\hbar\frac{\partial\rho}{\partial t} = [H_0 - \mathbf{d}\cdot\mathbf{E}, \rho], \tag{7}$$

where H_0 is the Hamiltonian of the lasing ions, without the three radiative processes mentioned above. $-\mathbf{d}\cdot\mathbf{E}$ is the interaction between the XRL field and the medium, in the dipole approximation.

As pointed above, the XRL beam propagation is roughly parallel to the z axis, even in the presence of refraction (paraxial approximation). In fact, the z coordinate varies by approximately 1 cm, while x and y vary only by a few tens of micrometers. The z axis is therefore chosen as quantization axis. At high XRL intensities, the occupation number of each energy level (αJ)—where J stands for the total angular momentum and α for the other quantum specifications (electronic configuration and so on)—has to be replaced by density matrix elements. Because of the nature of linearly propagating radiation, oscillations of the electric field occur in the plane perpendicular to the direction of propagation. In the saturation regime, the interaction between $\mathbf{E}$ and each individual state $|\alpha JM\rangle$ (Zeeman sublevel) is then, in general, different for each state. As a consequence, one can no longer define an occupation number for (αJ) to which rates of stimulated emission or absorption are associated. In the saturation regime, one is then faced with calculations of fractional populations of Zeeman sublevels, $\langle JM|\rho|JM\rangle$, rather than of the (αJ) level populations. It is worth stressing that the Zeeman sublevels belonging to any (αJ) level remain degenerate. The corresponding populations are affected by two opposite effects, namely, saturation effect and elastic collisions between free electrons and lasing ions. The first effect is responsible for differences between the populations of sublevels differing by their $|M|$ value, while elastic collisions tend to restore equilibrium between these populations (see Appendix B).

From Eqs. (6) and (7), it is straightforward to derive (i) the radiative transfer equation and (ii) rate equations for sublevels involved in the investigated line. We have

$$\frac{\mathbf{k}}{k}\cdot\nabla I_{\pm}(\nu,\mathbf{r},t) = \epsilon_{\pm}(\nu,\mathbf{r},t) + G(\nu,\mathbf{r},t)I_{\pm}(\nu,\mathbf{r},t), \tag{8}$$

where $I_{\pm}$ is the contribution to the intensity involving all $\Delta M=\pm 1$ transitions. The corresponding emissivity, in the small solid angle Ω, and the gain coefficient take the following forms:

$$\epsilon_{\pm}(\nu,\mathbf{r},t) = \frac{3\Omega}{8\pi}(2J+1)A_{ul}h\nu\Phi_{ul}(\nu)\sum_M N_{\alpha JM}(\mathbf{r},t) \times \begin{pmatrix} J & 1 & J' \\ -M & \pm 1 & M \mp 1 \end{pmatrix}^2, \tag{9}$$

$$G(\nu,\mathbf{r},t) = 3\hbar k(2J+1)B_{ul}\Phi_{ul}(\nu)\sum_M [N_{\alpha JM}(\mathbf{r},t) - N_{\alpha' J'(M-1)}(\mathbf{r},t)]\begin{pmatrix} J & 1 & J' \\ -M & 1 & M-1 \end{pmatrix}^2, \tag{10}$$

where $u=(\alpha J)$ and $l=(\alpha' J')$ are the upper and lower lasing levels, respectively. Concerning the 0-1 transition in Ni-like ions, we have $\alpha=(1s^2 2s^2 2p^6 3s^2 3p^6)3d^9 4d$, $\alpha'=(1s^2 2s^2 2p^6 3s^2 3p^6)3d^9 4p$, $J=0$, and $J'=1$. The N's now designate population densities of Zeeman sublevels.

One has to consider two sets of rate equations. The first set governs the populations of all nonlasing levels. To first order, these populations are insensitive to the saturation effect. The second set describes the evolution of the sublevels $(|\alpha JM\rangle)$ and $(|\alpha' J' M'\rangle)$ population densities. It contains rate equations with an explicit dependence on the intensity of the XRL beam. Furthermore, these rate equations involve diagonal elements of ρ (n_{JM} and $n_{J'M'}$) and off-diagonal elements called coherences. In fact, since the wave vector $\mathbf{k}$ is nearly parallel to the z axis, $\mathbf{E}$ can be expressed as an incoherent sum of the two circularly polarized components σ_+ and σ_-. As a result, only the coherences $\langle J'M-1|\rho|JM\rangle$ and $\langle J'M+1|\rho|JM\rangle$ are excited. The coherences $\langle J'M-1|\rho|JM\rangle$ are excited only by σ_+ fields and the coherences $\langle J'M+1|\rho|JM\rangle$ only by σ_- fields. It is worth noting that $\sigma_\pm$ involves either an emission with $\Delta M=\pm 1$ or an absorption with $\Delta M=\mp 1$. However, following Degl'Innocenti [25], we have checked that these coherences are negligible due to the smallness of the Bohr frequency associated with the two lasing levels, compared to the Einstein coefficient for spontaneous emission. The rate equations then take the following forms:

$$\frac{\partial}{\partial t}n_{\alpha JM}(\mathbf{r},t) = r_{\alpha JM}(\mathbf{r},t) - R_{\alpha JM}(\mathbf{r},t)n_{\alpha JM}(\mathbf{r},t) - \sum_{q=\pm 1}\langle JM|d_q|J'M-q\rangle^2 \times [n_{\alpha JM}(\mathbf{r},t) - n_{\alpha' J' M-q}(\mathbf{r},t)] \times \frac{1}{2\hbar^2\epsilon_0 c}\int d\nu\, I_q(\nu,\mathbf{r},t)\Phi_{ul}(\nu) \tag{11}$$

for the upper sublevels and

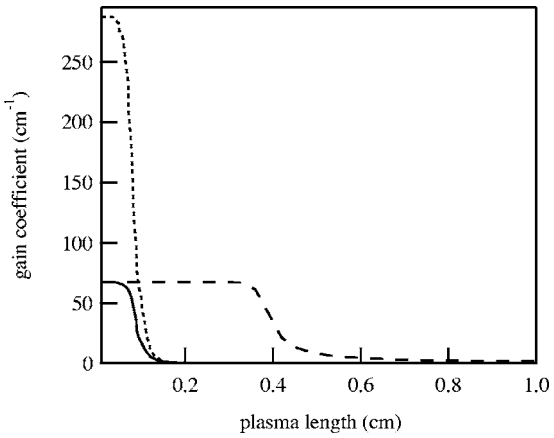

FIG. 6. Gain coefficient of the 14.7 nm line in Ni-like Pd, as a function of plasma length. First approach, dotted curve. Second approach, without refraction, dashed curve; with refraction, full curve. Rays are launched at the time and from the cell of peak gain. Small-signal gain, electron density, and electron and ion temperature values at the onset of amplification, as in Fig. 4.

$$\frac{\partial}{\partial t} n_{\alpha' J' M'}(\mathbf{r},t) = r_{\alpha' J' M'}(\mathbf{r},t) - R_{\alpha' J' M'}(\mathbf{r},t) n_{\alpha' J' M'}(\mathbf{r},t) + \sum_{q=\pm 1} \langle JM' + q | d_q | J' M' \rangle^2 \times [n_{\alpha J M' + q}(\mathbf{r},t) - n_{\alpha' J' M'}(\mathbf{r},t)] \times \frac{1}{2\hbar^2 \epsilon_0 c} \int d\nu \, I_q(\nu,\mathbf{r},t) \Phi_{ul}(\nu) \qquad (12)$$

for the lower sublevels. The r and R coefficients arise from all populating and depopulating processes, except those of absorption and induced emission. The last contribution in the right-hand side of both equations is due to the saturation effect.

The radiative transfer and the two sets of rate equations are solved consistently. The ray path is partitioned into a succession of p adjacent intervals $[s_{i-1}, s_i]$ of width Δs, where $i=1,\ldots,p$ with $s_0=0$ and $s_p=L$. The intervals are taken sufficiently small, so that gain and emissivity can be assumed homogeneous in each one of them. We then have $G=G_i$ and $\epsilon=\epsilon_i$ for s between s_{i-1} and s_i. Equation (8) is then easily solved, giving the intensity for a propagation length in the range $[s_{i-1}, s_i]$.

The small-signal gain obtained from intensity measurements is equal to 65 cm^{-1}. Figure 6 shows the variation of the gain coefficient with plasma length. The MB approach gives a small-signal gain equal to 67 cm^{-1}, in good agreement with experiment, while the first approach gives more than 250 cm^{-1}. The good agreement with the MB approach is due to a better treatment of the saturation effect. The difference between the dotted curve (first approach) and dashed curve (second approach) shows the importance of a good description of saturation. As seen from a comparison between the two calculations using the paraxial MB formalism (dashed curve and full curve), refraction plays an important role because high gains reside in a tiny region (~ 10 μm).

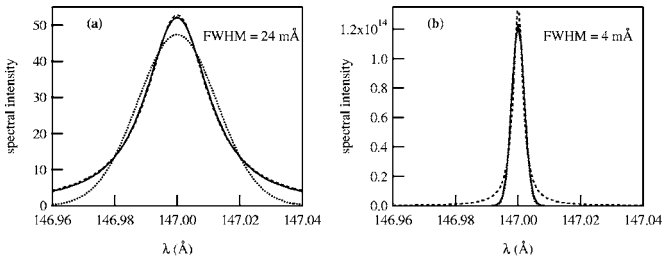

FIG. 7. As in Fig. 5.

Figure 7 represents the intensity spectrum calculated for two plasma lengths. At the beginning of the amplification [$L=0.1$ mm, Fig. 7(a)] the shape is Lorentzian, and for a larger L value, the shape nears a Gaussian, as in the first approach. The width at the exit from the plasma is again equal to 4 mÅ.

A rapid comparison between the two approaches shows that they both provide the same line shape and the same width for the output. The paraxial MB approach is more satisfactory because it has the advantage to provide more realistic gain and integrated intensity values. In fact, the agreement with the measured gain is good, contrary to the first approach.

B. Longitudinal coherence

The spectral shape of the output is Gaussian with a FWHM of 4 Å. In this case (see Appendix A), the profile of the self-coherence also has a Gaussian shape. The coherence time τ_{coh} is defined by $\Gamma(\tau_{\mathrm{coh}})=\Gamma(\tau=0)/e$. The coherence length, defined by $l_{\mathrm{coh}}=c\tau_{\mathrm{coh}}$, is equal to 290 μm. The agreement with the experiment performed at Lawrence Livermore laboratory is satisfactory. The small discrepancy could be due to the range of validity of the Wiener-Khintchine (WK) theorem. In fact, the WK theorem is used both in modeling and in experiment. In modeling, we calculate the spectral intensity and FWHM, and the WK theorem allows us to obtain Γ and the longitudinal coherence length. In the experiment, one measures the visibility as a function of the time delay, and the WK theorem (indirectly) yields the FWHM. One has to be cautious when utilizing the WK theorem because it involves stationary fields.

IV. CONCLUDING REMARKS

We have modeled the experiment performed at the Lawrence Livermore National Laboratory on the temporal coherence of the Ni-like Pd XRL at wavelength 14.7 nm. In order to account rigorously for saturation and refraction, we have used the paraxial MB formalism to study level populations and gain coefficient in the saturation regime, and coupled the associated code to a ray-trace code. Since the rays experience variable temperatures and electron density, the gain and emissivity have to be updated during propagation. This is done by adding into the MB code a subroutine giving the spontaneous emission line profile.

While the XRL intensity spectrum is Lorentzian at the beginning of amplification, due to the importance of homo-

geneous broadening, it becomes Gaussian at the exit from plasma, similarly to experiment. The calculated FWHM is equal to 4 mÅ while the indirectly measured width is ~2.9 mÅ. The calculated coherence length is equal to 290 μm, while the length derived from visibility measurements is 400 μm. The small discrepancy between the calculated and measured coherence lengths could be due, at least in part, to the range of validity of the Wiener-Khintchine theorem which involves stationary fields. In fact, the experimental width of the XRL pulse was derived from visibility measurements, assuming implicitly that $\mathbf{E}(t)$ is a stationary and ergodic field. Unfortunately, due to the short duration of XRL pulses in the transient pumping scheme, the field is far from being stationary. A new definition of the energy spectrum of a nonstationary ensemble of pulses (see, e.g., Ref. [26]) would improve the agreement between theory and experiment.

ACKNOWLEDGMENTS

We are grateful to G. J. Pert (York University) for providing the hydrodynamic-atomic code EHYBRID. One of us (D.B.) is indebted to R. F. Smith, J. Dunn (Lawrence Livermore National Laboratory, California), A. Calisti (PIIM, Marseille), and B. Rus (PALS Centre, Prague) for fruitful discussion during this work.

APPENDIX A: SELF-COHERENCE AND COHERENCE LENGTH

Let us consider the spectral density $S(\nu)$, normalized in the sense that $\int_{-\infty}^{\infty} S(\nu)d\nu=1$.

If we assume a Gaussian shape for $S(\nu)$, we can write

$$S(\nu) = G \exp\left[-\left(\frac{\nu}{\nu_D}\right)^2\right],$$

where $\nu_D=\Delta\nu_D/2\sqrt{\ln 2}$ and $G=1/\sqrt{\pi}\nu_D$. Following the Wiener-Khintchine theorem [23], the self-coherence function is written as

$$\Gamma(\tau) = 2\int_{-\infty}^{\infty} S(\nu)\exp(-i\pi\nu\tau)d\nu = 2\int_{-\infty}^{\infty} S(\nu)\cos(2\pi\nu\tau)d\nu - 2i\int_{-\infty}^{\infty} S(\nu)\sin(2\pi\nu\tau)d\nu. \quad \text{(A1)}$$

The integral involving the sine is obviously null. Following Ref. [21], we then have

$$\Gamma(\tau) = 2\exp(-\pi^2\tau^2\nu_D^2). \quad \text{(A2)}$$

The shape of the self-coherence is also Gaussian. The coherence time τ_{coh} is defined as the time delay for which self-coherence (or visibility) is reduced by a factor $1/e$. We then have

$$\tau_{coh} = \frac{1}{\pi\nu_D} = \frac{2\sqrt{\ln 2}}{\pi\Delta\nu_D}. \quad \text{(A3)}$$

The coherence length is defined as $l_{coh}=c\tau_{coh}$.

Let us now consider the spectral density described by the normalized Lorentzian shape:

$$S(\nu) = L\frac{\nu_L^2}{\nu^2+\nu_L^2},$$

where $L=1/\pi\nu_L$ and $\nu_L=\Delta\nu_L/2$. Equation (A1) then gives

$$\Gamma = \frac{4}{\pi}\int_0^{\infty}\frac{1}{1+t^2}\cos(mt)dt,$$

where $t=\nu/\nu_L$ and $m=2\pi\tau\nu_L$. Following Ref. [21], we easily obtain

$$\Gamma(\tau) = 2\exp(-2\pi\tau\nu_L). \quad \text{(A4)}$$

The coherence time is now

$$\tau_{coh} = 1/(2\pi\nu_L) = 1/(\pi\Delta\nu_L). \quad \text{(A5)}$$

In conclusion, we can write the coherence length as

$$l_{coh} = A\frac{c}{\pi\Delta\nu}, \quad \text{(A6)}$$

where $A=2\sqrt{\ln 2}$ if the intensity spectrum presents a Gaussian shape and 1 in the case of a Lorentzian shape.

APPENDIX B: INFLUENCE OF ELASTIC COLLISIONS ON POPULATIONS

Let us attribute the (αJ) label to the two lasing levels. The spontaneous emission is known to be isotropic, and we reasonably assume that the electron-ion collisions (elastic or inelastic) also verify this proprerty, yielding $r_{\alpha JM}=r_{\alpha J-M}$ and $R_{\alpha JM}=R_{\alpha J-M}$, where r and R are the coefficients introduced in Eqs. (11) and (12). Moreover, without injected polarized radiation, the integrals

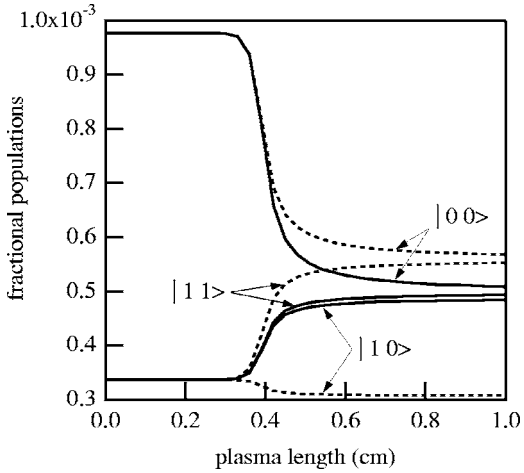

FIG. 8. Fractional populations n_{JM} of the $|JM\rangle$ Zeeman sublevels involved in the 0-1 line of Ni-like Pd, as a function of plasma length. Dashed curves, elastic collisions ignored; full curves, elastic collisions taken into account. Conditions of calculations are identical to those of Fig. 6.

$$\int d\nu I_q(\nu,\mathbf{r},t)\Phi_{ul}(\nu)$$

appearing in Eqs. (11) and (12) do not depend on q. The systems of rate equations for the two groups of Zeeman sublevels $\{|JM\rangle\}_{M\geqslant 0}$ and $\{|JM\rangle\}_{M\leqslant 0}$ are then identical. Solving the rate equations we need to consider only one sign, and we obtain fractional populations such that $n_{JM}=n_{J-M}$.

When the intensity of the x-ray beam increases, the difference of populations between Zeeman sublevels differing by their $|M|$ value increases (saturation effect). However, elastic collisions $|\alpha JM\rangle+e^-\rightarrow|\alpha JM'\rangle+e^-$ $(M\neq M')$ tend to restore equilibrium between the sublevels populations. An estimation of the elastic collision rate can be obtained from the formula [27]:

$$\Gamma \approx 3.87\times 10^{-6} N_e Z T_e^{-3/2} \ln\Lambda$$

where Γ is in s^{-1}, N_e in cm^{-3}, and T_e in eV. $\ln\Lambda$ is the Coulomb logarithm.

Figure 8 shows the variation with plasma length of the fractional populations of the $|00\rangle$, $|11\rangle$, and $|10\rangle$ Zeeman sublevels involved in the 0-1 line. We have $n_{11}=n_{1-1}$. As clearly seen, elastic collisions tend to balance the populations of the lower lasing level $(J=1)$. The difference $n_{11}-n_{10}$ is very small compared to the case where elastic collisions are ignored. Elastic collisions also affect the population of the upper lasing level $(J=0)$, but this is a second-order effect. In fact, variation of n_{11} and n_{1-1} has an effect on n_{00}, due to inelastic collisions and radiative processes. The gain coefficient depends on $n_{00}-n_{11}$. Since this difference has similar values whether or not elastic collisions are taken into account, the gain coefficient does not change.

[1] B. Rus, T. Mocek, A. R. Präg, M. Kozlová, G. Jamelot, A. Carillon, D. Ros, D. Joyeux, and D. Phalippou, Phys. Rev. A **66**, 063806 (2002).

[2] P. V. Nickles, V. N. Shlyaptsev, M. Kalachnikov, M. Schnürer, I. Will, and W. Sandner, Phys. Rev. Lett. **78**, 2748 (1997).

[3] G. J. Tallents, J. Y. Lin, J. Zhang, A. Behjat, A. Demir, M. M. Güzegöz, C. L. S. Lewis, A. MacPhee, D. Neely, G. J. Pert, R. Smith, J. S. Wark, P. J. Warwick, and E. Wolfrum, in *Applications of High Field and Short Wavelengths Sources*, OSA Technical Digest Series, edited by L. DiMauro, M. Murnane, and A. L'Huillier (Optical Society of America, Washington, D.C., 1997), p. 59.

[4] J. Nilsen and J. Dunn, Proc. SPIE **4505**, 100 (2001).

[5] J. Kuba, R. F. Smith, D. Benredjem, C. Möller, L. Upcraft, R. King, A. Klisnick, L. Drška, G. J. Pert, and J.-C. Gauthier, J. Opt. Soc. Am. B **20**, 208 (2003).

[6] F. Yan, J. Zhang, X. Lu, and J. Y. Zhong, Phys. Plasmas **11**, 3380 (2004).

[7] D. Benredjem, C. Möller, J. Dubau, J. Kuba, R. F. Smith, and C. Mossé, Phys. Rev. A **72**, 013821 (2005).

[8] G. Hazak and A. Bar-Shalom, Phys. Rev. A **38**, 1300 (1988).

[9] A. Sureau and P. B. Holden, Phys. Rev. A **52**, 3110 (1995).

[10] L. B. Da Silva, T. W. Barbee, Jr., R. Cauble, P. Celliers, D. Ciarlo, S. Libby, R. A. London, D. Matthews, S. Mrowka, J. C. Moreno, D. Ress, J. E. Trebes, A. S. Wan, and F. Weber, Phys. Rev. Lett. **74**, 3991 (1995).

[11] G. Jamelot, D. Ros, A. Carillon, B. Rus, T. Mocek, M. Kozlová, A. R. Präg, D. Joyeux, D. Phalippou, M. Boussoukaya, M. Kalmykow, F. Ballester, and E. Jacques, J. Appl. Phys. **98**, 044308 (2005).

[12] J. Dunn, R. F. Smith, J. Nilsen, A. J. Nelson, T. W. Van Buuren, S. J. Moon, J. R. Hunter, J. Filevitch, J. J. Rocca, M. C. Marconi, and V. N. Shlyaptsev, in *X-Ray Lasers 2002*, edited by J. J. Rocca, J. Dunn, and S. Suckewer, AIP Conf. Proc. No. 641 (AIP, Melville, NY, 2002), p. 481.

[13] J. E. Trebes, S. B. Brown, E. M. Campbell, D. L. Matthews, D. G. Nilson, G. F. Stone, and D. A. Whelan, Science **238**, 517 (1987).

[14] B. Rus, G. Jamelot, H. Bercegol, M. Kozlová, T. Mocek, P. Hormel, J. Polan, M. Stupka, K. Cassou, S. Kazamias, A. Klisnick, D. Ros, C. Danson, and S. Hawkes, Proc. SPIE **5919**, 59190K (2005).

[15] A. Klisnick, O. Guilbaud, D. Ros, K. Cassou, S. Kazamias, G. Jamelot, J.-C. Lagron, D. Joyeux, D. Phalippou, Y. Lechantre, M. Edwards, P. Mistry, and G. J. Tallents, J. Quant. Spectrosc. Radiat. Transf. **99**, 370 (2006).

[16] P. Celliers, F. Weber, L. B. Da Silva, T. W. Barbee, Jr., R. Cauble, A. S. Wan, and J. C. Moreno, Opt. Lett. **20**, 1907 (1995).

[17] R. F. Smith, J. Dunn, J. R. Hunter, J. Nilsen, S. Hubert, S. Jacquemot, C. Remond, R. Marmoret, M. Fajardo, P. Zeitoun, L. Vanbostal, M. F. Ravet, and F. Delmotte, Opt. Lett. **28**, 1 (2003).

[18] G. J. Pert, J. Fluid Mech. **131**, 401 (1983).

[19] I. P. Grant, Adv. Phys. **19**, 747 (1970).

[20] W. L. van Wyngaarden, K. Bhadra, and R. J. W. Henry, Phys. Rev. A **20**, 1409 (1979).

[21] *Handbook of Mathematical Functions*, edited by M. Abramowitz and I. A. Stegun (Dover, New York, 1970).

[22] J. Humlicek, J. Quant. Spectrosc. Radiat. Transf. **27**, 437 (1982).

[23] M. Born and E. Wolf, *Principles of Optics*, 7th ed. (Cambridge University Press, Cambridge, England, 1999).

[24] D. Attwood, *Soft X-rays and Extreme Ultraviolet Radiation: Principles and Applications* (Cambridge University Press, Cambridge, England, 1999).

[25] E. Landi Degl'Innocenti, Sol. Phys. **91**, 1 (1984).

[26] S. A. Ponomarenko, G. P. Agarwal, and E. Wolf, Opt. Lett. **29**, 394 (2004).

[27] J. L. Delcroix and A. Bers, *Physique des Plasmas* (InterEditions/CNRS Editions, Paris, 1994).